

Supporting Information

Active Coarsening of Binary Liquids with Active Rotation

Syeda Sabrina, Matthew Spellings, Sharon C. Glotzer, Kyle J. M. Bishop

Contents

1	Description of the movies	2
1.1	Movie 1: Strong damping – passive coarsening	2
1.2	Movie 2: Weak damping – active coarsening	2
1.3	Movie 3: Zero damping – active coarsening	2
1.4	Movie 4: Zero damping – vortex doublet	2
1.5	Movie 5: Microscopic model – active coarsening	2
2	Numerical integration	3
2.1	Stream function formulation	3
2.2	Fourier spectral method	3
2.3	Time stepping	3
2.4	Finite-size effects	4
3	Pair correlation function	5
4	Counting vortices in the vortex doublet regime	6
5	Vortex doublet on an infinite domain	7
5.1	Hydrodynamic model	7
5.2	Boundary integral formulation	7
5.3	Numerical implementation	8
5.4	Steady vortex doublet	8
6	Particle-based simulations	11
6.1	Microscopic model details	11
6.2	Connection between microscopic and continuum model	11

1 Description of the movies

1.1 Movie 1: Strong damping – passive coarsening

Passive coarsening in actively rotating liquids under strong rotation and strong damping for parameters $\alpha = 10$, $\beta = 10^2$, and $L = 1024$. The total duration of the simulation is $t = 10^5$; the time interval between frames is $\Delta t = 10^3$ with playback at 10 fps.

1.2 Movie 2: Weak damping – active coarsening

Active coarsening in actively rotating liquids under weak rotation and weak damping for parameters $\alpha = 10^{-2}$, $\beta = 10^{-3}$, and $L = 2048$. The total duration of the simulation is $t = 10^5$; the time interval between frames is $\Delta t = 500$ with playback at 7 fps.

1.3 Movie 3: Zero damping – active coarsening

Active coarsening in actively rotating liquids under weak rotation and no frictional damping for parameters $\alpha = 10^{-2}$, $\beta = 0$, and $L = 2048$. The total duration of the simulation is $t = 2.4 \times 10^4$; the time interval between frames is $\Delta t = 250$ with playback at 7 fps.

1.4 Movie 4: Zero damping – vortex doublet

Vortex doublet under strong rotation and no frictional damping for parameters $\alpha = 50$, $\beta = 0$, and $L = 256$. The total duration of the simulation is $t = 500$; the time interval between frames is $\Delta t = 0.5$ with playback at 10 fps.

1.5 Movie 5: Microscopic model – active coarsening

Active coarsening in spinners under weak rotation and weak damping for parameters $\alpha' = 0.25$, $\beta' = 0.01$, $N_s = 16,384$, packing fraction 0.5, and Brownian temperature 0.1. The total duration of the simulation is $t' = 10^5$; the time interval between the frames is $\Delta t' = 50$ with playback at 30 fps.

2 Numerical integration

2.1 Stream function formulation

As described in the main text, the equations governing the evolution of the compositional order parameter $\varphi(x, y)$ and the fluid velocity $\mathbf{v}(x, y)$ are

$$\frac{\partial \varphi}{\partial t} + \mathbf{v} \cdot \nabla \varphi = \nabla^2(-\varphi + \varphi^3 - \nabla^2 \varphi), \quad (1)$$

$$0 = -\nabla p + \nabla^2 \mathbf{v} + \alpha \nabla \times (\varphi \mathbf{e}_z) - \beta \mathbf{v}, \quad (2)$$

$$0 = \nabla \cdot \mathbf{v}. \quad (3)$$

To solve these equations numerically, it is convenient to introduce the stream function ψ where $\mathbf{v} = \nabla \times (\psi \mathbf{e}_z)$ such that the continuity equation (3) is satisfied automatically. Substituting this expression for the velocity into equation (2) and taking the curl of each term, we obtain

$$0 = \nabla^4 \psi + \alpha \nabla^2 \varphi - \beta \nabla^2 \psi. \quad (4)$$

Given the instantaneous composition $\varphi(x, y)$, equation (4) is solved for the stream function ψ and thereby the velocity $\mathbf{v}(x, y)$, which influences the evolution of the composition through equation (1).

2.2 Fourier spectral method

The governing equations (1) and (4) are solved numerically using semi-implicit Fourier spectral method on a 2D periodic domain [1]. In Fourier space, these equations become

$$\frac{\partial \Phi(\mathbf{k}, t)}{\partial t} + (ik_x \{v_x \varphi\}_{\mathbf{k}} + ik_y \{v_y \varphi\}_{\mathbf{k}}) = -k^2 \{\varphi^3 - \varphi\}_{\mathbf{k}} - k^4 \Phi(\mathbf{k}, t), \quad (5)$$

$$0 = k^4 \Psi(\mathbf{k}, t) - \alpha k^2 \Phi(\mathbf{k}, t) + \beta k^2 \Psi(\mathbf{k}, t), \quad (6)$$

where $\{ \}_{\mathbf{k}}$ denotes the Fourier transform with wave vector \mathbf{k} ; $\Phi(\mathbf{k}, t) = \{\varphi(\mathbf{r}, t)\}_{\mathbf{k}}$ and $\Psi(\mathbf{k}, t) = \{\psi(\mathbf{r}, t)\}_{\mathbf{k}}$ correspond to the transformed compositional field and stream function, respectively. Equation (6) can be solved directly to obtain the stream function as a function of the composition field

$$\Psi(\mathbf{k}, t) = \frac{\alpha}{(k^2 + \beta)} \Phi(\mathbf{k}, t). \quad (7)$$

The Fourier transform of the velocity field \mathbf{V} is computed as $V_x = ik_y \Psi$ and $V_y = -ik_x \Psi$; the velocity \mathbf{v} is then obtained by taking the inverse Fourier transform.

2.3 Time stepping

Equation (5) is integrated in time using a semi-implicit scheme [1] whereby the highest order derivatives are computed implicitly while the remaining non-linear terms are computed explicitly. The first order scheme (used only for the initial time step) is given by

$$(1 + \Delta t k^4) \Phi^{n+1} = \Phi^n - \Delta t k^2 \{\varphi^3 - \varphi\}_{\mathbf{k}}^n - \Delta t (ik_x \{v_x \varphi\}_{\mathbf{k}}^n + ik_y \{v_y \varphi\}_{\mathbf{k}}^n), \quad (8)$$

where Δt is the (constant) time step, and n is a time index ($t_n = n\Delta t$). Subsequent time steps are performed using the following second order, Adams-Bashforth Backward Differentiation (AB2/BDF2) scheme

$$(3 + 2\Delta t k^4) \Phi^{n+1} = 4\Phi^n - \Phi^{n-1} - 2\Delta t [2(k^2 \{\varphi^3 - \varphi\}_{\mathbf{k}}^n + ik_x \{v_x \varphi\}_{\mathbf{k}}^n + ik_y \{v_y \varphi\}_{\mathbf{k}}^n) - (k^2 \{\varphi^3 - \varphi\}_{\mathbf{k}}^{n-1} + ik_x \{v_x \varphi\}_{\mathbf{k}}^{n-1} + ik_y \{v_y \varphi\}_{\mathbf{k}}^{n-1})]. \quad (9)$$

At each time step, the stream function and the velocity are computed using equation (7), and the compositional field is updated using equation (9).

2.4 Finite-size effects

The results presented in the main text do not depend on the simulation size L and are therefore representative of an arbitrarily large domain. To show this, we considered simulations of different sizes to determine conditions under which the finite size of the simulation domain is or is not significant (Figure 1). To summarize, a finite simulation domain is an effective approximation for an infinite domain provided $R < 0.1L$ and – in the case of the vortex doublet regime – $N_v > 10$, where N_v is the number of vortices.

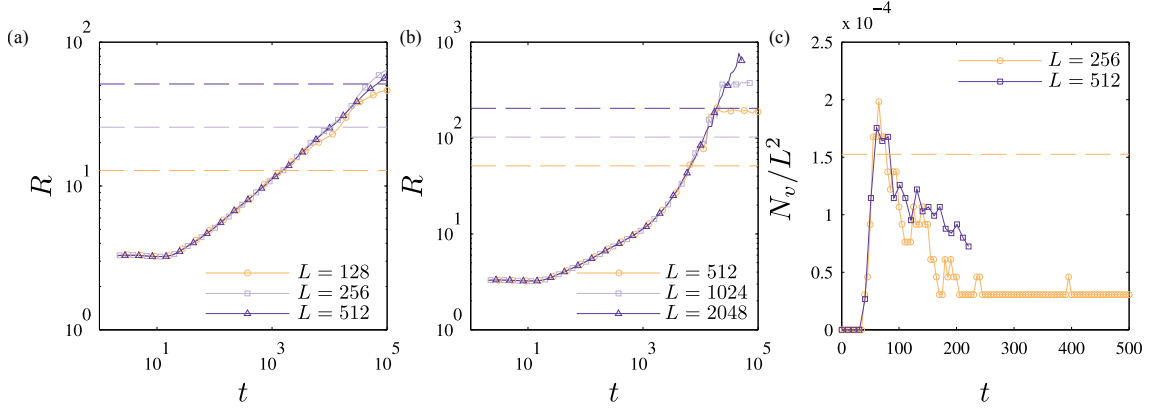


Figure 1: Finite-size effects. **(a)** Domain size R as a function of time for three different simulation sizes L with parameters $\alpha = 10$ and $\beta = 10^2$ corresponding to passive coarsening. The dashed lines correspond to $R = 0.1L$, above which the results are influenced by the finite size of the simulation cell. **(b)** Domain size R as a function of time for three different L with parameters $\alpha = 10^{-2}$ and $\beta = 0$ corresponding to active coarsening. Again, the dashed lines correspond to $R = 0.1L$. **(c)** In the vortex doublet regime, the number density of vortices (N_v/L^2) evolves in time independent of the simulation size L provided $N_v > 10$ (dashed line). Here, the parameters are $\alpha = 50$ and $\beta = 0$.

3 Pair correlation function

The pair correlation function is defined as

$$G(\mathbf{r}) = \int \varphi(\mathbf{r}')\varphi(\mathbf{r}' + \mathbf{r})d\mathbf{r}', \quad (10)$$

which is subsequently normalized such that $G(0) = 1$. In practice, this quantity can be computed efficiently using the convolution theorem as

$$\{G(\mathbf{r})\}_{\mathbf{k}} = \{\varphi(\mathbf{r})\}_{\mathbf{k}}^* \{\varphi(\mathbf{r})\}_{\mathbf{k}}, \quad (11)$$

where $\{ \}_{\mathbf{k}}$ denotes the Fourier transform, and $*$ the complex conjugate. Averaging over all orientations, we obtain the radially averaged pair correlation function denoted $g(r)$. The figures below illustrate the evolution of $g(r)$ for both passive and active coarsening.

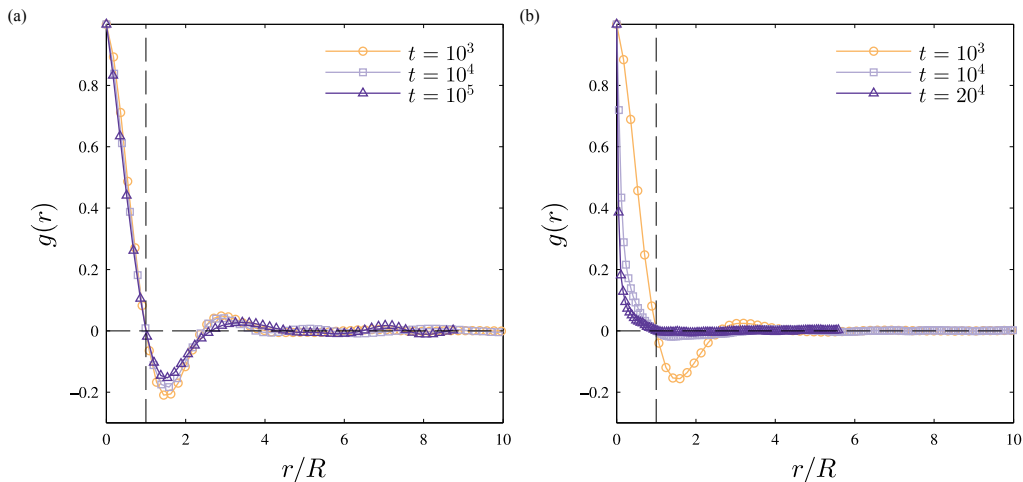


Figure 2: Radially averaged pair correlation function $g(r)$ vs. r/R where R is the domain size – defined as the first root of $g(r)$. **(a) Passive coarsening.** For parameters $\alpha = 10$, $\beta = 10^2$, and $L = 1024$, the domains grow in time *via* passive diffusive coarsening; the pair correlation function is approximately self-similar at different times when scaled by R . **(b) Active coarsening.** For parameters $\alpha = 10^{-2}$, $\beta = 0$, and $L = 2048$, domains grow in time *via* active convective coarsening; the pair correlation function is no longer self-similar.

4 Counting vortices in the vortex doublet regime

Figure 5b in the main text presents the number of vortices $N_v(t)$ as a function of time; here, we describe how $N_v(t)$ was determined from the transient composition field $\varphi(x, y, t)$. Specifically, a vortex is defined as a contiguous region in which the local composition satisfies $|\varphi| > 0.3$. This threshold value was chosen to most clearly distinguish vortex regions enriched with like-rotating particles ($\varphi \sim \pm 1$) from their well-mixed surroundings ($\varphi \sim 0$). Figure 3 shows the distribution of local compositions at three different times. At early times, the system is homogeneous with a single peak at $\varphi \approx 0$. Following vortex nucleation, the distribution becomes trimodal with new peaks at $\varphi \approx \pm 0.7$ corresponding to the unmixed interiors of the vortices.

Additionally, we count only those vortex regions that are larger than a certain critical area, $A > A^* = 138$. Without this condition, the number of vortices is dominated by small regions with $|\varphi| > 0.3$ that appear and disappear erratically due to the swirling motions of larger vortices.

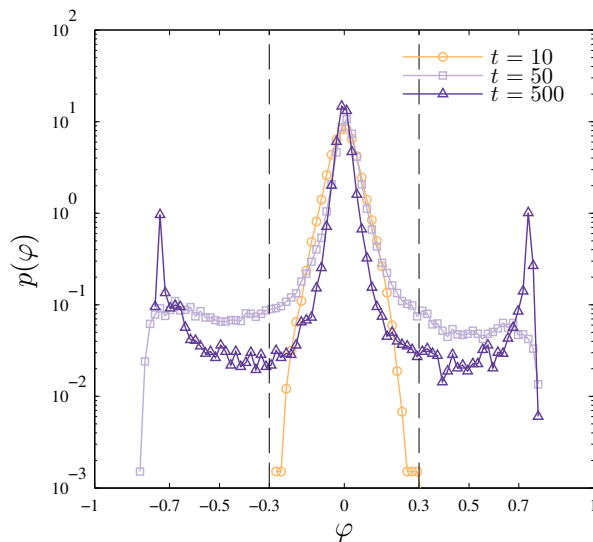


Figure 3: Distribution of the composition φ at three different times in the vortex doublet regime with parameters $\alpha = 50$, $\beta = 0$, and $L = 256$.

5 Vortex doublet on an infinite domain

Here, we determine the flow due to a single vortex doublet moving within an unbounded 2D domain. Base on the simulation results presented in the main text, a vortex doublet can be approximated by two fluid drops that are driven to move by a uniform stress acting at their respective surfaces. We use the boundary integral method to simulate the dynamics of the drop interfaces and compute the steady-state flow field.

5.1 Hydrodynamic model

Starting from equation (6) in the main text (with $Re \rightarrow 0$ and $Ca^{-1} \rightarrow 0$), the velocity field is governed by

$$0 = -\nabla p + \nabla^2 \mathbf{v} + \alpha \nabla \times (\varphi \mathbf{e}_z) - \beta \mathbf{v}, \quad (12)$$

$$0 = \nabla \cdot \mathbf{v}. \quad (13)$$

Vortex doublets are observed when active rotation is strong ($\alpha \gg 1$) and frictional damping is absent ($\beta \rightarrow 0$). The compositional order parameter is assumed to be $\varphi \approx \pm 1$ inside the vortex drops that make up the doublet and $\varphi \approx 0$ outside of the drops. Furthermore, the characteristic size of the drops a is assumed to be much larger than the thickness of the interface ($a \gg 1$). Under these conditions, the Péclet number is large ($Pe = \alpha a \gg 1$) and diffusive transport can be neglected on the time scales of interest. Similarly, the area of the vortex drops, which grow in time via diffusive transport, are assumed to be constant.

With these assumptions, we can move from the phase-field model described in the main text to a multiphase hydrodynamic model characterized by three fluids – the two counter-rotating drops which are separated from the surrounding fluid by sharp interfaces. The motion of each fluid is governed by the 2D Stokes equation

$$0 = -\nabla p + \nabla^2 \mathbf{v} = \nabla \cdot \boldsymbol{\sigma}, \quad (14)$$

since $\varphi \approx \text{constant}$ in each fluid domain. Integrating equation (12) over the drop interface, we obtain the following jump condition on the stress

$$(\mathbf{n} \cdot \boldsymbol{\sigma})_{out} - (\mathbf{n} \cdot \boldsymbol{\sigma})_{in} = \mathbf{T} \quad (15)$$

where \mathbf{n} is the unit normal vector directed from outward from the drop surface, and \mathbf{T} is the surface stress due to active rotation

$$\mathbf{T} = \alpha \varphi_{in} \mathbf{t}. \quad (16)$$

Here, \mathbf{t} is the unit vector tangent to the interface with the convention $\mathbf{n} \times \mathbf{t} = \mathbf{e}_z$, and $\varphi_{in} = \pm 1$ denotes the direction of active rotation within the drop.

5.2 Boundary integral formulation

The Stokes flow at \mathbf{x} due to a point force \mathbf{f} at \mathbf{y} in an otherwise quiescent fluid is given by

$$\mathbf{v}(\mathbf{x}) = \mathbf{f} \cdot \mathbf{G}(\mathbf{x} - \mathbf{y}), \quad (17)$$

where $\mathbf{G}(\mathbf{x} - \mathbf{y})$ is the Green's function for Stokes flow in 2D

$$\mathbf{G}(\mathbf{r}) = \frac{1}{4\pi} \left[- \left(\ln r + \frac{3}{2} \right) \mathbf{I} + \frac{\mathbf{r}\mathbf{r}}{r^2} \right], \quad (18)$$

and $\mathbf{r} = \mathbf{x} - \mathbf{y}$ [2]. Using this Green's function solution, the velocity due to a vortex doublet can be expressed as

$$\mathbf{v}(\mathbf{x}) = \int_S \mathbf{T}(\mathbf{y}) \cdot \mathbf{G}(\mathbf{x} - \mathbf{y}) dS_y, \quad (19)$$

where the integral is carried out over the surface of the two drops. The fluid motion induced by the active stress at the drop surface cause the interface to move and deform according to the kinematic relation

$$\frac{d\mathbf{x}_s}{dt} = \mathbf{v}(\mathbf{x}_s), \quad (20)$$

where \mathbf{x}_s is a point on the drop surface. Together equations (18) – (20) specify a free boundary problem governing the evolution of the shape and position of the active drops. Scaling lengths by the characteristic drop size a , stresses by α , and velocities by αa , the above problem contains no additional parameters.

5.3 Numerical implementation

The integral equation above is solved numerically using an iterative solution procedure made up of three components: (i) describing the drop interface; (ii) calculating the surface velocity; (iii) advancing the drop interface in time [3].

As illustrated in Figure 4, we consider the dynamics of a single vortex doublet, which is symmetric with respect to reflection about the 2-axis. Consequently, we need only describe the shape of one of the two vortex drops that comprise the doublet. The drop shape is described using $N = 40$ discrete points, which are fitted with cubic splines, $\mathbf{x}_s(s)$, using the arclength s as the dependent variable. This approach provides a twice differentiable representation of the drop interface, which is convenient for computing the unit normal and tangent vectors.

The fluid velocity at each of the N points is then computed by integrating over the drop surface using equation (19). Integration over each of the N segments of the boundary is performed using a 4-point Gaussian quadrature scheme. No special treatment is given to the logarithmic singularities encountered during the integration as these occur only at boundaries between the segments.

Finally, the drop interface is advanced forward in time using a two-step Adams-Bashforth scheme. We adopt a Eulerian view point whereby marker points on the drop interface are advanced using only the normal component of the velocity, $v_n = \mathbf{n} \cdot \mathbf{v}$. Marker points are updated in time as

$$\mathbf{x}_s^{j+1} = \mathbf{x}_s^j + \Delta t \left[\frac{3}{2} \mathbf{n} v_n(\mathbf{x}_s^j) - \frac{1}{2} \mathbf{n} v_n(\mathbf{x}_s^{j-1}) \right], \quad (21)$$

where Δt is a fixed time step (typically, $\alpha \Delta t = 0.01$). For long simulation times, the marker points tend to cluster together, and it is necessary to periodically redistribute them over the surface of the drop. Additionally, owing to the approximate nature of the numerical scheme, the drop area is not exactly constant in time, and it is therefore necessary to periodically rescale the the drop to maintain a constant area.

5.4 Steady vortex doublet

Figure 4 shows the shape and the corresponding flow field of a single vortex doublet at steady-state. Here, the area of each drop is πa^2 , where a is the radius of the initially circular drops. The doublet moves at a steady velocity of $\mathbf{U} = -0.196\alpha a \mathbf{e}_2$.

Far from the doublet, the velocity disturbance can be approximated by Taylor expanding the Green's function in equation (19) about its center at \mathbf{x}_0

$$v_l(\mathbf{x}) - U_l = F_i^{(0)} G_{il} + F_{ij}^{(1)} \frac{\partial}{\partial y_j} G_{il} + \frac{1}{2} F_{ijk}^{(2)} \frac{\partial}{\partial y_k} \frac{\partial}{\partial y_j} G_{il} + \dots, \quad (22)$$

where the Greens function $\mathbf{G}(\mathbf{x} - \mathbf{y})$ and its derivatives are evaluated at $\mathbf{y} = \mathbf{x}_0$. The moments of

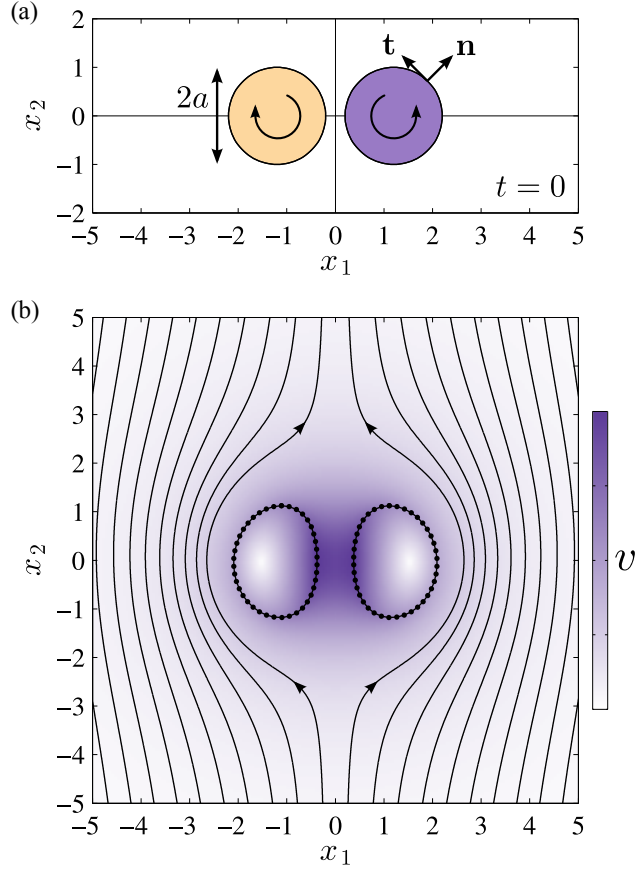


Figure 4: **(a)** Initial configuration of a single vortex doublet on an infinite 2D domain. The left drop is driven to rotate in the clockwise direction; the right in the counter clockwise direction. **(b)** Steady-state configuration of the two active drops as described by the boundary integral method using $N = 40$ marker points on the surface of each drop. Streamlines are shown in black and the colormap shows the magnitude of the velocity vector \mathbf{v} .

this expansion are defined as

$$F_i^{(0)} = \int_S (n_l T_{li}) dS_y, \quad (23)$$

$$F_{ij}^{(1)} = \int_S (n_l T_{li} r_j) dS_y, \quad (24)$$

$$F_{ijk}^{(2)} = \int_S (n_l T_{li} r_j r_k) dS_y, \quad (25)$$

where $\mathbf{r} = \mathbf{y} - \mathbf{x}_0$, and the integral is carried out over the surface of both drops that make up the vortex doublet. The zeroth moment – corresponding to the net force on the doublet – is identically zero. Owing to the symmetry of the doublet about $x_1 = 0$, the first moment is symmetric with $F_{ij}^{(1)} = 0$ for $i \neq j$. Consequently, there is no net torque on the doublet; however, there can be a finite stresslet. Symmetry also requires that the only nonzero elements of the second moment are $F_{112}^{(2)} = F_{121}^{(2)}$, $F_{211}^{(2)}$, and $F_{222}^{(2)}$; the particular form of the active stress (proportional to the tangent vector \mathbf{t}) further implies that $F_{222}^{(2)} = 0$.

At steady-state, the doublet becomes symmetric also in the x_2 direction, and the first moment vanishes ($F_{ij}^{(1)} = 0$). This observation follows from the kinematic reversibility of Stokes flows – there exists another steady-solution when the fluid velocity at each point is reversed. Under these conditions, the velocity field simplifies to

$$v_1 = \frac{1}{4\pi r^6} \left[\left(6F_{112}^{(2)} + F_{211}^{(2)} \right) r_1^3 r_2 - \left(2F_{112}^{(2)} + 3F_{211}^{(2)} \right) r_1 r_2^3 \right], \quad (26)$$

$$v_2 = U + \frac{1}{8\pi r^6} \left[\left(-2F_{112}^{(2)} + F_{211}^{(2)} \right) r_1^4 + 6 \left(2F_{112}^{(2)} + F_{211}^{(2)} \right) r_1^2 r_2^2 - \left(2F_{112}^{(2)} + 3F_{211}^{(2)} \right) r_2^4 \right]. \quad (27)$$

The three parameters characterizing the flow field are computed numerically to be $U = 0.196\alpha a$, $F_{112} = -7.57\alpha a^3$, and $F_{211} = 15.1\alpha a^3$. As noted in the main text, the velocity disturbance due to the vortex double decays as $v \sim \alpha a^3/r^2$ and the associated stresses as $\tau \sim \alpha a^3/r^3$.

6 Particle-based simulations

6.1 Microscopic model details

Each disk of a spinner interacts *via* a purely repulsive Weeks-Chandler-Andersen contact potential shifted to the surface of the disk. In addition, to ensure phase separation in the absence of activity as the continuum model would exhibit, we add Gaussian attractions between the central disks of like-spinning spinners

$$U_{gauss} = \begin{cases} \epsilon \exp\left(-\frac{1}{2}\left(\frac{r}{\sigma_{gauss}}\right)^2\right) & r < r_{cut} \\ 0 & r \geq r_{cut} \end{cases} \quad (28)$$

where $\epsilon = 0.5k_B T$, $\sigma_{gauss} = 6\sigma$, and $r_{cut} = 60\sigma$.

6.2 Connection between microscopic and continuum model

To first approximation, the characteristic scales used in non-dimensionalizing the continuum model are analogous to those used in the microscopic model (Table 1). Consequently, the dimensionless coefficients such as the strength of the rotational driving torque and that of frictional drag in both models should be comparable to each other in an order-of-magnitude sense. In the main text, this is reflected by the use of common notation – that is, α and α' for the strength of rotation, β and β' for the strength of frictional drag in the continuum and the microscopic models, respectively.

The characteristic length scale used in the continuum model $(K/r)^{1/2}$, is the thickness of the interface separating the two counter-rotating domains. On the other hand, the size of the spinners, σ is used as unit of length in the microscopic model. We assume that these two lengths should be comparable to each other such that $(K/r)^{1/2} \sim \sigma$. Similarly, the characteristic time scales used in both models should be comparable to each other such that $K/Mr^2 \sim \sigma(m/(k_B T))^{1/2}$. Here, K/Mr^2 is the time of unmixing in the continuum model and $\sigma(m/(k_B T))^{1/2}$ is the time required for a spinner to diffuse one particle diameter in the microscopic model. Finally, the characteristic energy scale in the continuum model is taken to be ηMr and that in the microscopic model is $k_B T$. Approximating the fluid viscosity as $\eta \sim (mk_B T/\sigma^2)^{1/2}$ [4] and applying the two relations above, this energy scale becomes, $k_B T \sim \eta Mr$.

	Continuum	Microscopic
length	$(K/r)^{1/2}$	σ
time	K/Mr^2	$\sigma(m/(k_B T))^{1/2}$
energy	ηMr	$k_B T$

Table 1: Characteristic scales used in non-dimensionalizing the continuum and the microscopic models.

References

- (1) J. Zhu, L. Q. Chen, J. Shen and V. Tikare, *Phys. Rev. E*, 1999, **60**, 3564–3572.
- (2) C. Pozrikidis, *Boundary integral and singularity methods for linearized viscous flows*, Cambridge University Press, New York, 1992.
- (3) J. Tazosh, M. Manga and H. A. Stone, in *Int. Conf. Bound. Elem. Technol.* 1992, pp. 20–39.
- (4) R. García-Rojo, S. Luding and J. J. Brey, *Physical Review E*, Dec. 2006, **74**, 061305.